Experimental and Computational Investigation of Microbubble Formation in a Single Capillary Embedded T-junction Microfluidic Device

Aaqib H. Khan[#], Arijit Ganguli[†], Mohan Edirisinghe[‡], and Sameer V. Dalvi[#]*

Chemical Engineering, Indian Institute of Technology Gandhinagar, Palaj, Gandhinagar - 382355, Gujarat, India

† School of Engineering and Applied Sciences, Ahmedabad University, Ahmedabad-380009, Gujarat, India

‡ Department of Mechanical Engineering, University College London (UCL), London WC1E 7JE, U.K.

***E-mail: sameervd@iitgn.ac.in; Phone: 091-79-2395 2408**

Abstract: In recent years, there has been a notable increase in the interest towards microfluidic devices for microbubble synthesis. The upsurge can be primarily attributed to the exceptional control these devices offer in terms of both the size and size distribution of microbubbles. Among various microfluidic devices available, capillary-embedded T-junction microfluidic (CETM) devices have been extensively used for synthesis of microbubbles. One distinguishing feature of CETM devices from conventional T-junction devices is the existence of a wall at the rightmost end, which causes a backflow of the continuous phase at the mixing zone during microbubble formation. The back flow at the mixing zone can have several implications during microbubble formation. It can possibly affect the local velocity and shearing force at the mixing zone, which, in turn, can affect the size and production rate of the microbubbles. Therefore, in this work we experimentally and computationally understand the process of microbubble formation in CETM devices. The process is modelled using computational fluid dynamics (CFD) with the volume-of-fluid approach, which solves the Navier-Stokes equations for both the gas and liquid phases. Three

scenarios with a constant liquid velocity of 0.053 m/s with varying gas velocity and three with a constant gas velocity of 0.049 m/s at different liquid velocity were explored. Increase in the liquid and gas velocity during microbubble formation was found to enhance production rates in both experiments and simulations. Additionally, the change in microbubble size with the change in liquid velocity was found to agree closely with the findings of the simulation with a coefficient of variation of 10%. When plotted against the time required for microbubble generation, the fluctuations in pressure showed recurrent crests and troughs throughout the microbubble formation process. The understanding of microbubble formation in CETM devices in presence of backflow will allow improvement in size reduction of microbubbles.

Keywords: Microbubbles; Microfluidics; Computation Fluid Dynamics; Modelling, Microbubble Pinch-off.

Introduction: Microbubbles are micron-sized gas bubbles suspended in an aqueous media that are stabilised by shell material such as proteins [1], lipids [2, 3], and polymers [4]. Microbubbles are widely used in biomedical applications such as targeted drug [5, 6] or gene delivery [7] and ultrasound contrast imaging[8-10]. Microfluidic technology is one of the most promising tools to generate microbubbles due to its capability of consistently generating monodisperse microbubbles[11, 12]. However, the size of the microbubbles produced in microfluidic devices is critically dependent on the size capillaries used[13]. Based on the flow geometries and the contacting patterns of liquid and gaseous streams, microfluidic devices are classified as flow-focusing[14, 15] co-flow focusing [16], and T-junction microfluidics[17, 18]. Regardless of the type of microfluidic device being used, the formation of microbubbles is caused by the instability of the interface between gas and liquid phase [19]. This results in the gaseous stream routinely separated into gas pockets, which then get encased in an aqueous solution of protein or lipid to produce bubbles [20]. Interfacial forces have a substantial impact on microbubble generation when employing microfluidic devices[21]. The influence of interfacial forces can be defined by dimensionless numbers, such as the $Capillary\ no.\ (Ca) = \frac{\mu u}{\sigma}$, which is the ratio of the "viscous force to the surface tension force"[22], and the $Weber\ no.\ (We) = \frac{\rho u^2 d}{\sigma}$, which is the ratio of the "inertia force to the surface tension force"[23].

A novel capillary embedded T-junction microfluidic (CETM) devices was first introduced by Pancholi et al. 2008[11]. The incorporation of capillary-embedded microfluidic devices, such as the one utilized in the study, offers distinct advantages in terms of robustness and ease of use compared to conventional T-junction devices. Extensive experimental work has been conducted using capillary embedded T-junctions microfluidic devices[24-28], with the primary objectives being to understand the role of flow parameters on microbubble production rates and microbubble size and enhance the stability of the microbubbles[26, 29, 30]. Recently, CETM devices have also been

employed for synthesis of scaffolds [31, 32]. Jiang et. al [27] and Wu et.al [33] combined CETM devices in series to experimentally investigate microbubble formation at different flow rates and gas pressures with the objective to reduce the final size of the microbubbles. Despite of numerous reports, the underlying mechanism of microbubble formation in CETM devices remains unclear. The estimates of local pressure and velocity in the micro capillaries during microbubble formation can offer a platform to understand CETM devices better.

The local velocity vectors can be estimated experimentally using tracer particles[34] or μ-particle image velocimetry [35] and the local pressure using Laplace pressure sensors (LPS)[36, 37]. Computationally, the velocity vectors and pressure can be estimated using computational fluid dynamics (CFD) simulations. In CFD, the Navier-Stokes and continuity equations are solved simultaneously with a governing equation for a function that represents the interface. Different approaches like the Volume of Fluid (VOF)[38-40], Level-Set (LS)[41] and Combined Level-Set and VOF (CLSVOF)[42] are available for this purpose. Out of the available techniques Volume of Fluid (VOF) is the most utilised technique for interface tracking in a microfluidic device[43-46].

CFD simulations in conventional T-junction microfluidic device for gas-liquid flows have focused on estimation of velocity and pressure distribution during bubble breakup [38, 47-49] in addition to estimation of microbubble production rate as a function of operating parameters. Arias and Montlaur[49] performed investigations for microbubble generation in air-water systems and reported change in production rate of the microbubbles as a function of superficial gas velocity (U_{SG}). Liu et al.[47] incorporated CFD to analyse bubble formation, estimate velocity and pressure distributions, and understand microbubble breakup in T-junction microfluidic device as a function of change in channel width ratio (w_0/w_1). Chang and Cai[50] conducted a comprehensive investigation to understand the effects of surface tension and gas-liquid flow ratios on microbubble

size and production rates. It is worth noting that the production of bubbles and the pinch-off mechanism in conventional T-junctions have been extensively explored in previous studies by various researchers [39, 51, 52]. From the review of the existing literature, it has become evident that the majority of research efforts have been concentrated on elucidating the mechanisms governing microbubble formation in conventional T-junction devices. Thus, the goal of this work is to broaden the understanding of microbubble production by investigating it in the context of capillary-embedded T-junction microfluidic (CETM) devices.

CETM devices employed for microbubble generation incorporates a cross flow contact of fluid phases but with a back flow of the continuous phase at the mixing zone. In contrast to a conventional cross-flow device that exhibits equal flow velocities from both liquid inlets, the CETM device features a single inlet and a back flow induced by the presence of a wall. During microbubble formation, this backflow at the mixing zone can have several implications. Firstly, unlike the conventional T-junction, it can disrupt the fluid behavior at the mixing zone by affecting the pinch-off process of gas slugs. This, in turn, can affect the local velocity and shearing force at the mixing zone, potentially impacting the size and production rate of the microbubbles. Therefore, the objective of the present work is (a) to experimentally and numerically determine the effect of operating parameters on production rates and microbubble size (b) numerically understand the role of pressure and velocity distribution during bubble formation and breakup. Six scenarios have been presented, three for constant liquid velocity at 0.053 m/s and three for constant gas velocity at 0.049 m/s. The significance of pressure and velocity distribution during bubble formation under various operating conditions, and the significance of right hand side velocity in the mixing zone during bubble formation is also presented. Variation in bubble size and rate of production for different liquid and gas velocities is also presented. Finally, microbubble formation in a

conventional T-junction and CETM devices with back flow is compared to understand the role of back flow during microbubble formation.

Methods and Materials

Materials: Bovine-serum-albumin (BSA) (quality >98%, as lyophilized powder) was purchased from Proliant Biologicals in New Zealand. Glutaraldehyde (GA, Grade 1, 25% in H_2O) was acquired from Sigma-Aldrich India. These were utilized without additional purification. Nitrogen gas (Ultrahigh pure grade) was bought from JP gas suppliers India to be used as a dispersed phase during the production of microbubbles.

Preparation of the aqueous solution: Aqueous phase for microbubble formation was made by dissolving 15% (w/w) BSA in deionized water for 1 hour at room temperature (25 °C) with steady magnetic stirring. The physicochemical properties of fluid phases are presented in table 1.

Experimental Setup for the production of microbubbles: The experimental setup includes a cross-flow type microfluidic T- junction custom manufactured from a poly (methyl methacrylate) (PMMA) block with dimensions of (20×20×10 mm) and 1.6 mm hollow channels. Capillaries made of Teflon Fluorinated Ethylene Polypropylene (TFEP) with an outer diameter (OD) of 1.6 mm and an inner diameter (ID) of 200 µm were inserted into the PMMA block. To prevent leakage, high-quality HPLC fittings were utilized to connect the tube to the PMMA block. To produce the cross-flow, a third capillary was added to the block, perpendicular to the other capillaries. The cross flow consists of an inlet for gas and aqueous phase each, a channel for outflow of bubbles after pinch off. Due to the relatively large OD of the capillary tube, a visible stagnant zone is created at the junction of the capillaries such that the zone is filled with liquid at all times and applies an addition pressure force or introduces back flow during microbubble formation. The schematic depiction of the experimental apparatus is shown in Fig. 1.

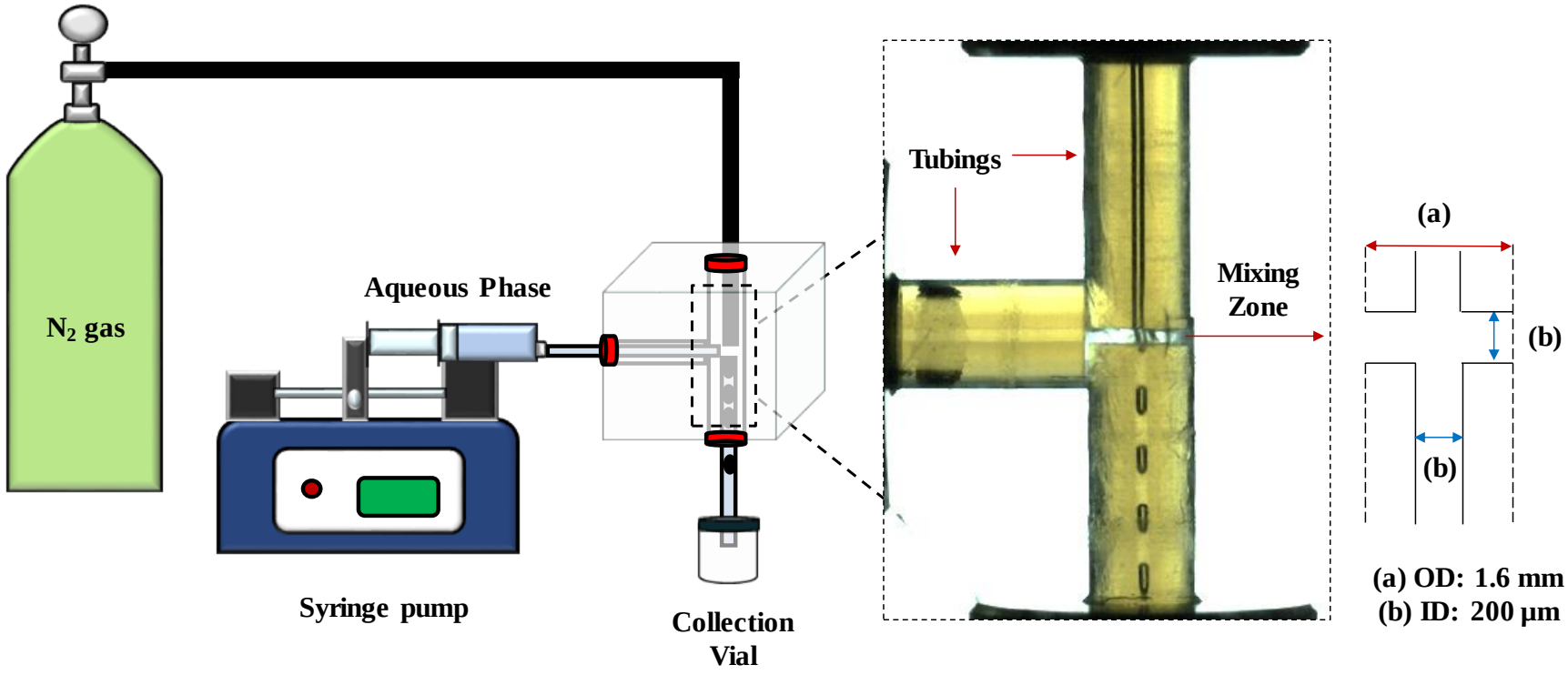

Figure 1. Schematic of the experimental setup and the geometric dimensions of the hollow capillary tubings used for microbubble generation. The outer diameter (a) and the inner diameter (b) of the tubings are 1.6 mm and 200 µm, respectively. Gas and liquid phase enter into the T-junction through the inner diameter of the tubings and meet at the mixing zone of height (b) for microbubble formation. The right-side of the mixing zone consists of a wall which induces back flow of the aqueous phase at the mixing zone during formation of microbubbles.

The CETM device was linked to a gas-regulator that was connected to the nitrogen gas tank. A digital pressure gauge was used to monitor the incoming gas pressure (EN-400, purchased from Adarsh Industries, Mumbai-India).

Table 1. Physicochemical properties of the fluid streams

Fluid Type	Surface Tension (mN/m)	Viscosity (mPas)	Density (Kg/m3)
BSA (Aqueous Phase)	53 ± 2.7	1.6 ± 0.25	1050 ± 8
N_2 (Gas Phase)	-	0.0176	1.16

To provide a non-pulsating liquid flow, the aqueous phase was injected into the T-junction using a Harvard Apparatus (PHD ultra) syringe pump. A high-speed camera (Photron FASTCAM Mini UX) was utilized to record the production of microbubbles in the T-junction operated at a frame rate of 4000 frames per second. The production rate of microbubble formation was estimated using high-speed videos by counting the number of microbubbles formed in the recorded frames. Equation 1 was used to obtain the production rate (bubbles per second).

$$\text{Bubble production rate (bubbles per sec)} = \frac{\text{Bubbles count}}{\text{Total number of frames}} \times \frac{\text{Frames}}{\text{sec}} \quad (1)$$

Mathematical modeling

Governing Equations

Table 2. Governing equation utilized for VOF simulations

Eq. No.	Type of equation	Expression
1.	Continuity	$\nabla \cdot \vec{v} = 0$
2.	Navier-Stokes	$\vec{v} \cdot \nabla \vec{v} = -\frac{1}{\rho}\nabla p + \vartheta \nabla^2 \vec{v}$
3.	Volume of fluid (VOF)	$\frac{\partial \varphi}{\partial t} + u \cdot \nabla \varphi = 0$

The governing equations used VOF simulation are presented in table 2. Here, $\vec{v}$ is the velocity vector, p is fluid pressure, ρ is the density, ϑ is the kinematic viscosity, and φ is the volume fraction

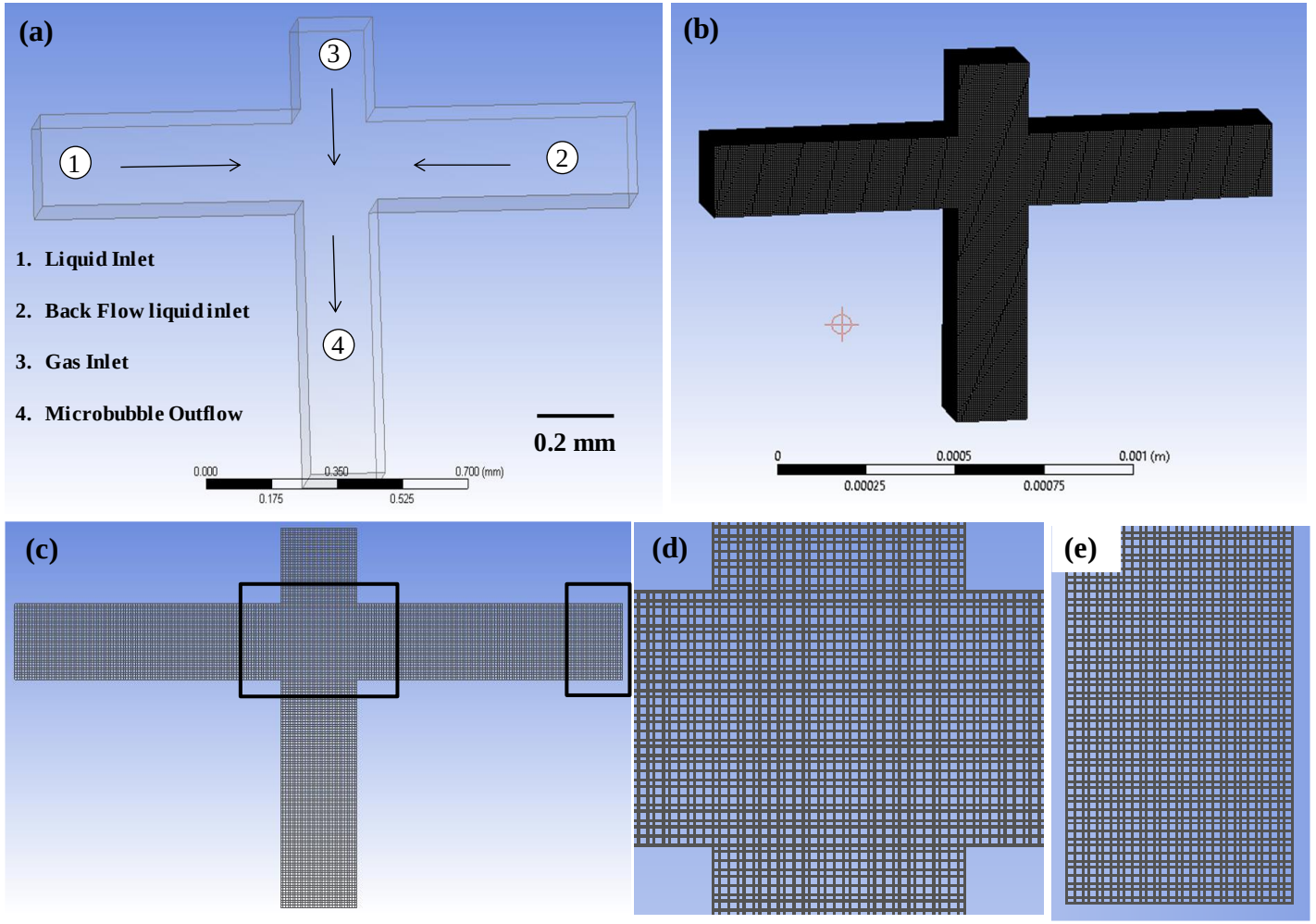

Figure 2. Computational domain for the microchannel (A) 3D Geometry with boundary conditions in Cartesian co-ordinates (B) 3D geometry with Hexahedral mesh (C) 2D geometry with Hexahedral mesh (D&E) Zoom View of the rectangle boxes highlighted in 2D geometry.

of a fluid phase. The CSF model of Brackbill et al.[53] was used to compute the surface tension force as a source term in the momentum equation for the cells containing the interface. The expression for surface tension force($\vec{F}$) is presented by;

$$\vec{F} = \sigma \frac{\rho k \, \hat{n}}{\frac{1}{2}\left(\rho_p + \rho_q\right)} \tag{2}$$

where σ is the coefficient of surface tension, $\hat{n}$ is the surface normal which is proportional to the gradient of volume fraction, κ is the local surface curvature calculated as follows (Brackbill et al.). p and q are the primary and secondary phases respectively.

$$\kappa = -\left(\nabla \hat{n}\right) = \frac{1}{|n|}\left[\frac{n}{|n|}\nabla|n| - \left(\nabla . n\right)\right]. \tag{3}$$

The geometric reconstruction scheme based on piecewise linear approach proposed by Rider & Kothe[54] was used for the reconstruction of the interface. In the VOF approach, the reconstructed interface is advected by solving an advection equation for the volume fraction of the secondary phase.

Geometric details and grid sensitivity: Fig. 2A shows the 3D geometry used for the simulations while Fig. 2B & 2C represents the corresponding grid used in 3D and 2D, respectively. And, Fig. 2D&E presents the zoom view of the corresponding grid. Fig. S1 shows the grid sensitivity for the case when the bubble formation starts at the neck (t = 0 seconds when bubble formation starts). The horizontal centerline from 1 to 2 (as per Fig. 2A) was chosen for the plot of velocity versus horizontal distance as shown in Fig. S1. The grid sensitivity was carried out for three different mesh elements namely 233280, 273310, 315570, 355570 and 435600 elements. It can be observed that the highest deviation between the mesh elements of coarser to medium meshes reduced from 27% to 4% (deviations between 233280 and 355570 was 27%, 273310 and 355570 was 12%,

315570 and 355570 was 4%) while that for the 355570 and 436500 was around 4%. Due to the lower deviation and lower computational cost associated with executing transient simulations compared to finer mesh under various flow conditions, the medium grid of mesh elements with 355570 elements was used for all numerical simulations presented in this work.

Method of solution and Boundary conditions: Both the faces on the right and left hand side of the horizontal limb and top of the central vertical limb shown in Fig. 2A have been modeled as velocity inlets. The outlet is represented as pressure outlet. All the other faces are modeled using the no-slip wall boundary condition. The spatial derivatives were discretized using the QUICK scheme [55] while a first-order implicit method was used for the discretization of the temporal derivatives. The Pressure Implicit with Splitting of Operator (PISO) algorithm [56] was used for the pressure-velocity coupling in the momentum equation.

Modeling the mixing zone: The experimental setup, as seen in Fig. 1, consists of a mixing zone. The mixing zone may be modelled as a horizontal liquid column with the liquid inlet on the left limb and the gas inlet perpendicular to the top in the center as shown in Fig. 2A. To accurately achieve the phenomenon of pinch off, it is necessary to simulate the right hand side (RHS) velocity, replicating the conditions found in the experimental observation. In order to obtain an initial estimate of RHS velocity, a simulation of single-phase flow in a horizontal rectangular channel with the same dimensions as the mixing zone has been performed, as shown in Fig. S2. The left side of the channel has been assigned a velocity inlet boundary condition, while the right side has been assigned a wall boundary condition. Subsequently, we determined the back pressure and velocity resulting from the presence of the wall. The results obtained from the simulated sample, with a liquid inlet velocity of 0.053 m/s, are illustrated in Fig. S2. The velocity resulting from backflow due to the wall was initially approximated to be ~ 0.02 m/s. The actual RHS velocity at

the junction during the process of microbubble formation is contingent to the hindrance caused by the developing gas microbubble. Therefore, for ease of simulation the velocity of the right-hand side (RHS) was established as velocity inlet boundary condition instead of a wall. The precise magnitude of the right-hand side (RHS) velocity was determined using an iterative procedure, beginning at a velocity of 0.02 m/s (velocity resulting from backflow due to the wall) and gradually increasing it until pinch-off takes place. Hence, the velocity on the right-hand side (RHS) is distinct for every gas and liquid velocity investigated in this study and was determined through an iterative procedure.

A dimensionless analysis by De Menech et al. (2008) suggested that flow through T-junctions are dependent on four dimensional parameters by Buckingham-Π analysis. These include Reynolds number (Re), Capillary number (Ca), viscosity ratio and velocity ratio (v). Velocity ratio (v) and flow ratio (Q) would be same, since the capillary diameter for both gas and liquid inlet are similar. Here, Re is in the range $4 < Re < 30$ and viscosity ratio are less than 1. The operating velocities were determined experimentally using a systematic approach, beginning with the minimal flow rates of both liquid and gas required to ensure stable microbubble production. Following that, the flow rates were gradually raised until the formation of microbubbles was no longer possible due to an excess of either liquid or gas flow. Velocity ratios considered for the present analysis are $0.3 < v_g / v_l < 2.64$ while variation in Ca is $0.0016 < Ca < 0.006$ for varying gas velocity and at a constant liquid velocity and vice-versa.

Results and discussion

Microbubble formation in T-junction microfluidic device: Fig. 1 presents the experimental setup used to generate microbubbles. A microfluidic device with a single T-junction enabling cross-flow contact between aqueous and gaseous phases was utilized. The aqueous phase was

composed of a 15% BSA solution, while the gaseous phase was composed of nitrogen gas (N_2). Microbubble generation occurred at the mixing zone primarily due to interfacial disturbances arising from viscosity difference and differential pressure effects. The increase in pressure forces at the gas-liquid interface may be ascribed to flow constraints experienced by the liquid stream due to simultaneous entry of gaseous stream into the exit channel. This detaching force, which is the result of the combined action of shearing force and squeezing pressure at the gas-liquid interface counteracts with the attaching force due to surface tension. Therefore, microbubble formation in microfluidic devices can be described as the result of detaching forces surpassing the attaching forces. This effect causes the gaseous stream to break-up into numerous tiny gas pockets, each surrounded by a pair of liquid droplets resulting in the formation of microbubbles.

Comparison of experimental and simulated microbubble pinch-offs: Change in liquid velocity at constant gas pressure and vice versa significantly affects the pinch-off process during microbubble formation. This not only changes the magnitude of forces acting at the cross flow junction but also drastically affects the microbubble production rates and microbubbles size[57]. Comparison of simulation and experimental microbubble formation for different flow velocities for liquid and gas phase is presented in Fig. 3-6. Figs. 3 (a-j) present sequential microbubble formation at distinct time intervals for the gas to liquid velocity ratio v (v_g / v_l) = 1 or v_g=0.049 m/s and v_l=0.053 m/s, comparing simulated and experimental microbubble formation process (Video S1). Initially, the gas stream extends downstream for a fixed period of time (~ 1 ms). Subsequently, the gas phase undergoes compression at the junction by the continuous liquid phase and the backflow, with a right-hand-side (RHS) velocity (v_{rh}) of 0.025 m/s. At t = 5 ms, the interface reaches the far end of the junction, with slight off-center, skewed towards the right of the junction. At 6 ms, a bubble emerges, as evidenced in the snapshots. The process of simulated and

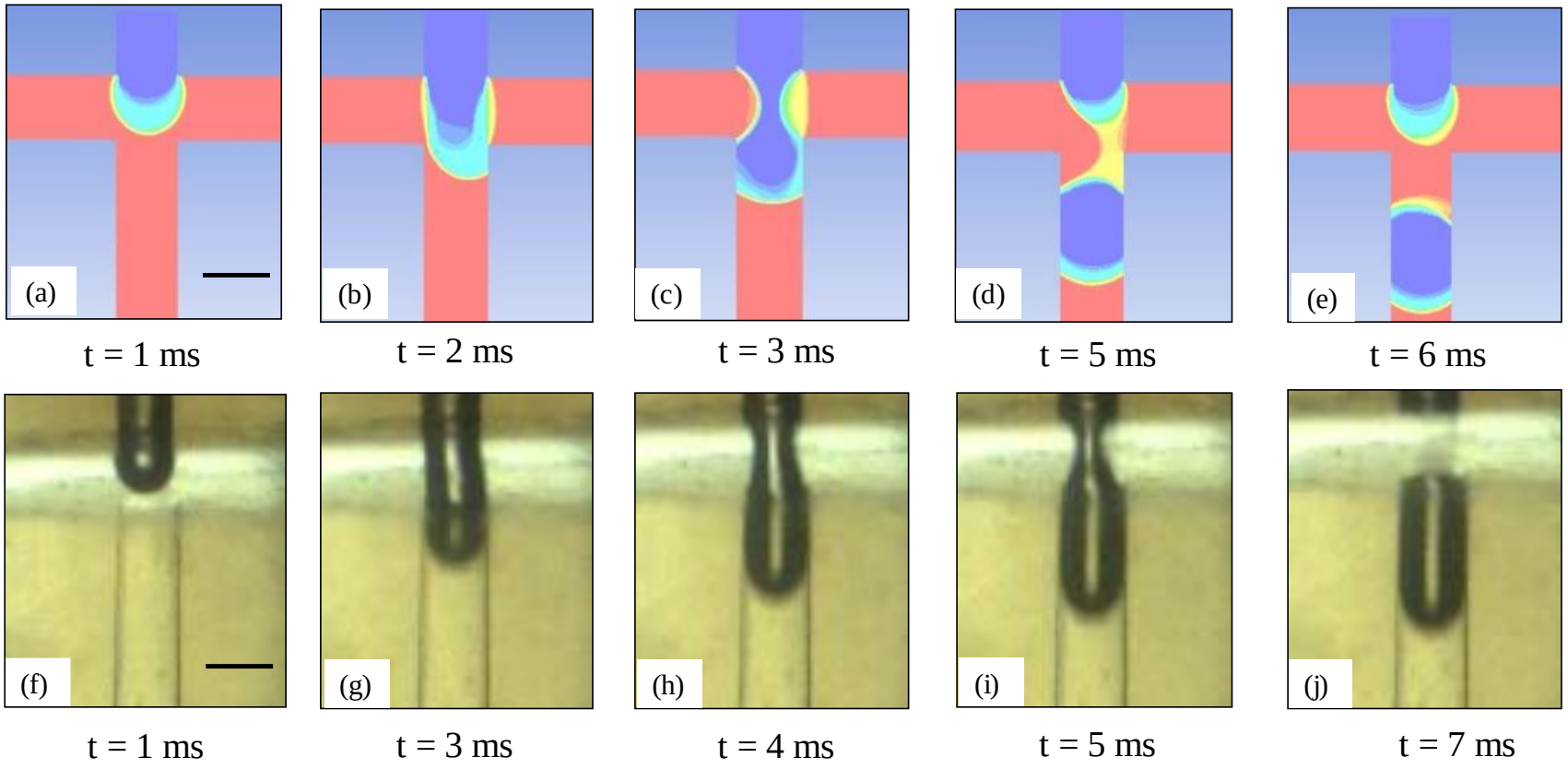

Figure 3. Snapshots of microbubble formation and pinch off process for v_g=0.049 m/s and v_l=0.05 m/s, v_{rh} (right) = 0.025 m/s, (a-e) CFD Simulation and (f-j) Experiment. Scale bar = 200µm.

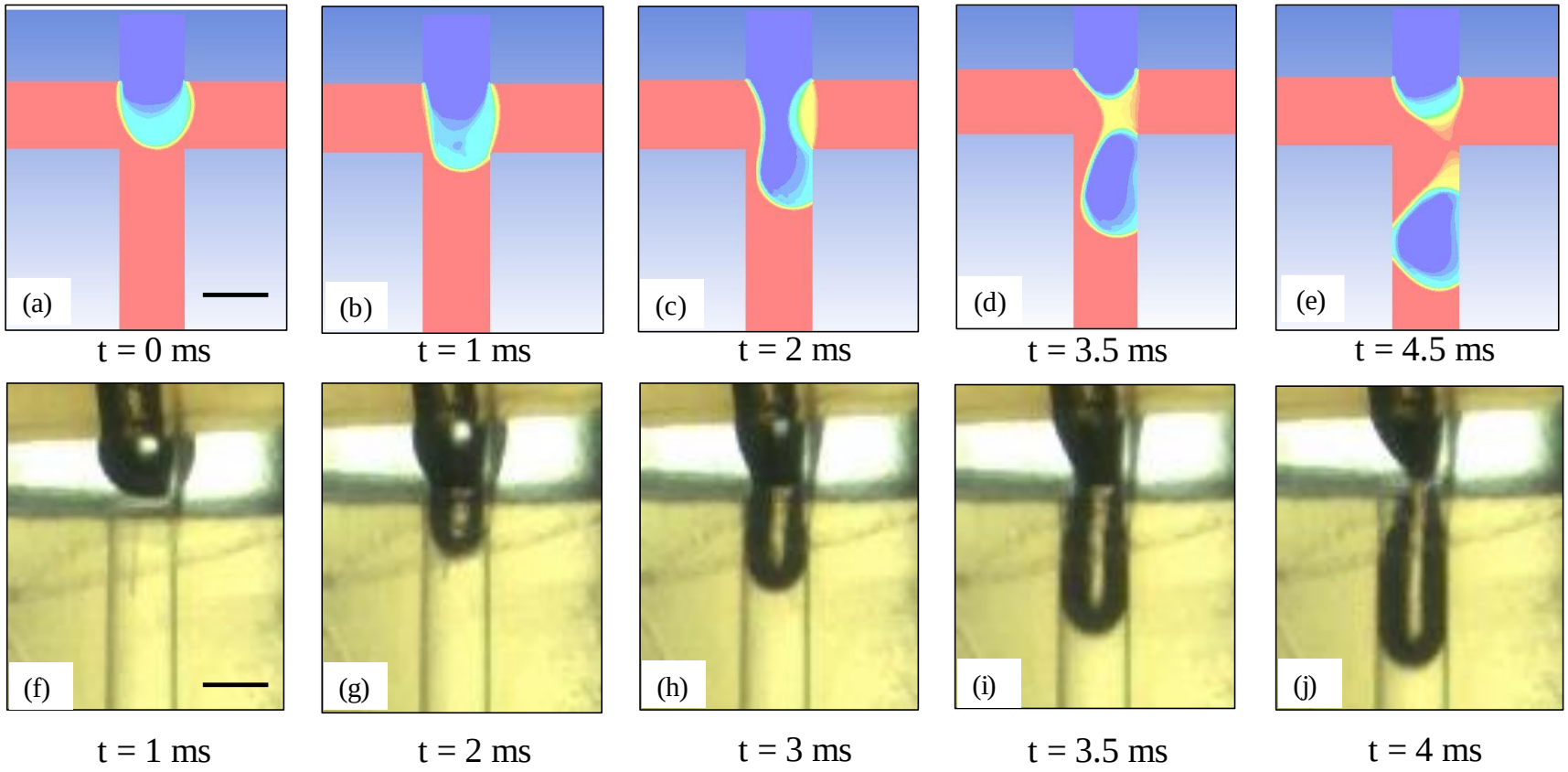

Figure 4. Snapshots of microbubble formation and pinch off process for v_g=0.049 m/s and v_l=0.159 m/s, v_{rh} (right) = 0.045 m/s, (a-e) CFD Simulation and (f-j) Experiment. Scale bar = 200µm.

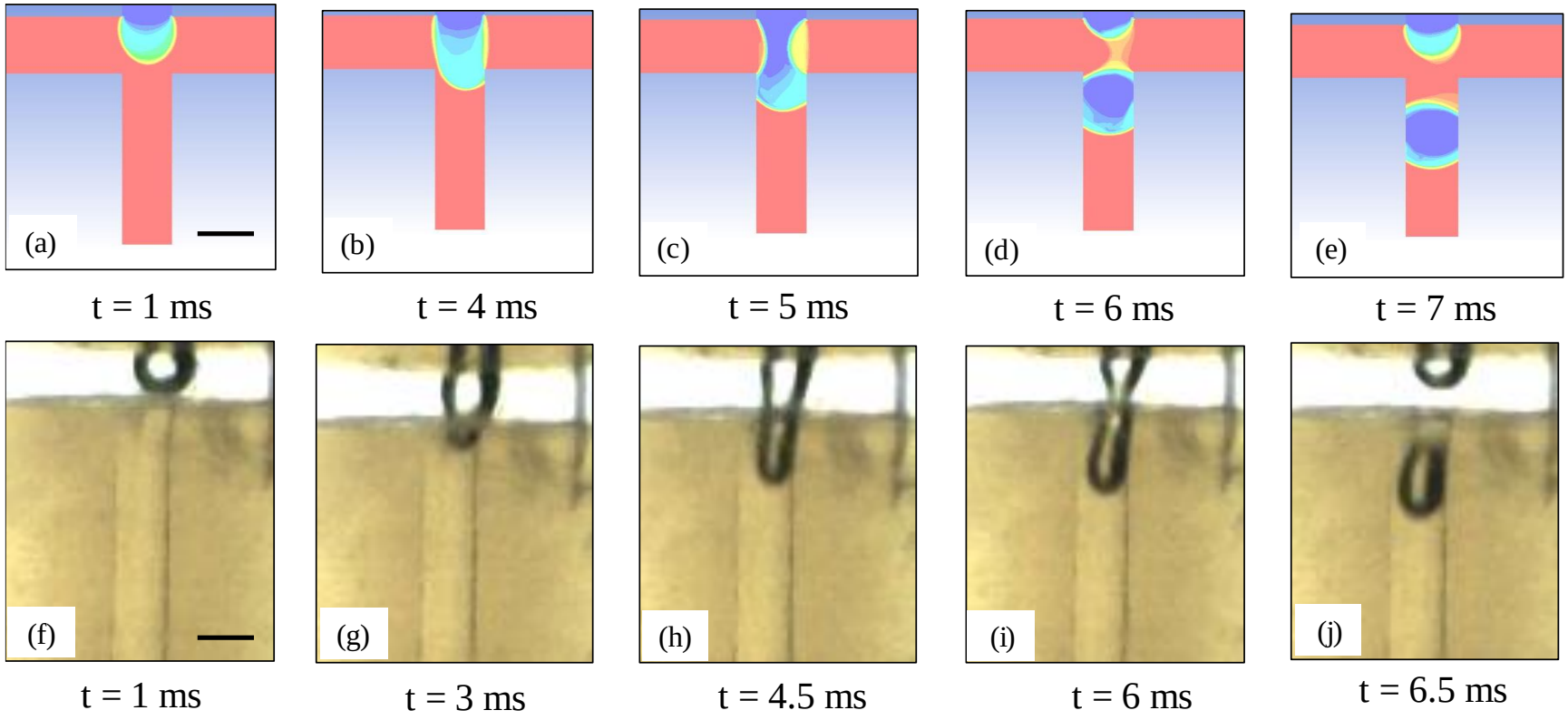

Figure 5. Snapshots of microbubble formation and pinch off process for v_g=0.027 m/s and v_l=0.053 m/s, v_{rh} (right) = 0.025 m/s, (a-e) CFD Simulation and (f-j) Experiment. Scale bar = 200µm.

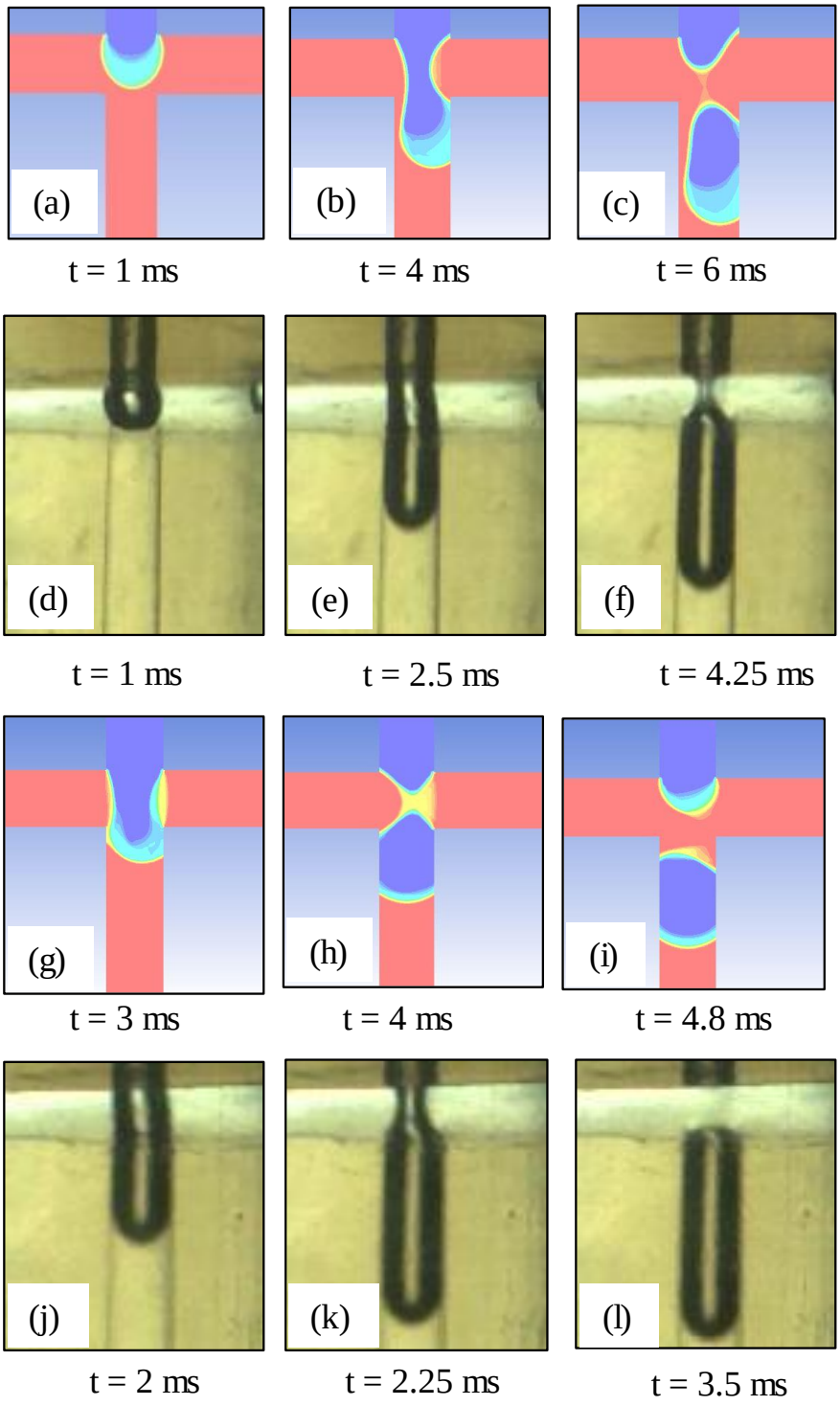

Figure 6. Volume fractions depicting typical bubble formation and pinch off process for v_g=0.049 m/s and v_l=0.079 m/s, v_{rh} (right) = 0.03 m/s (a-c) simulation and (d-f) experiment. Volume fractions depicting typical bubble formation and pinch off process for v_g=0.067 m/s and v_l=0.053 m/s, v_{rh} (right) = 0.025 m/s (g-i) simulation and (j-l) experiment.

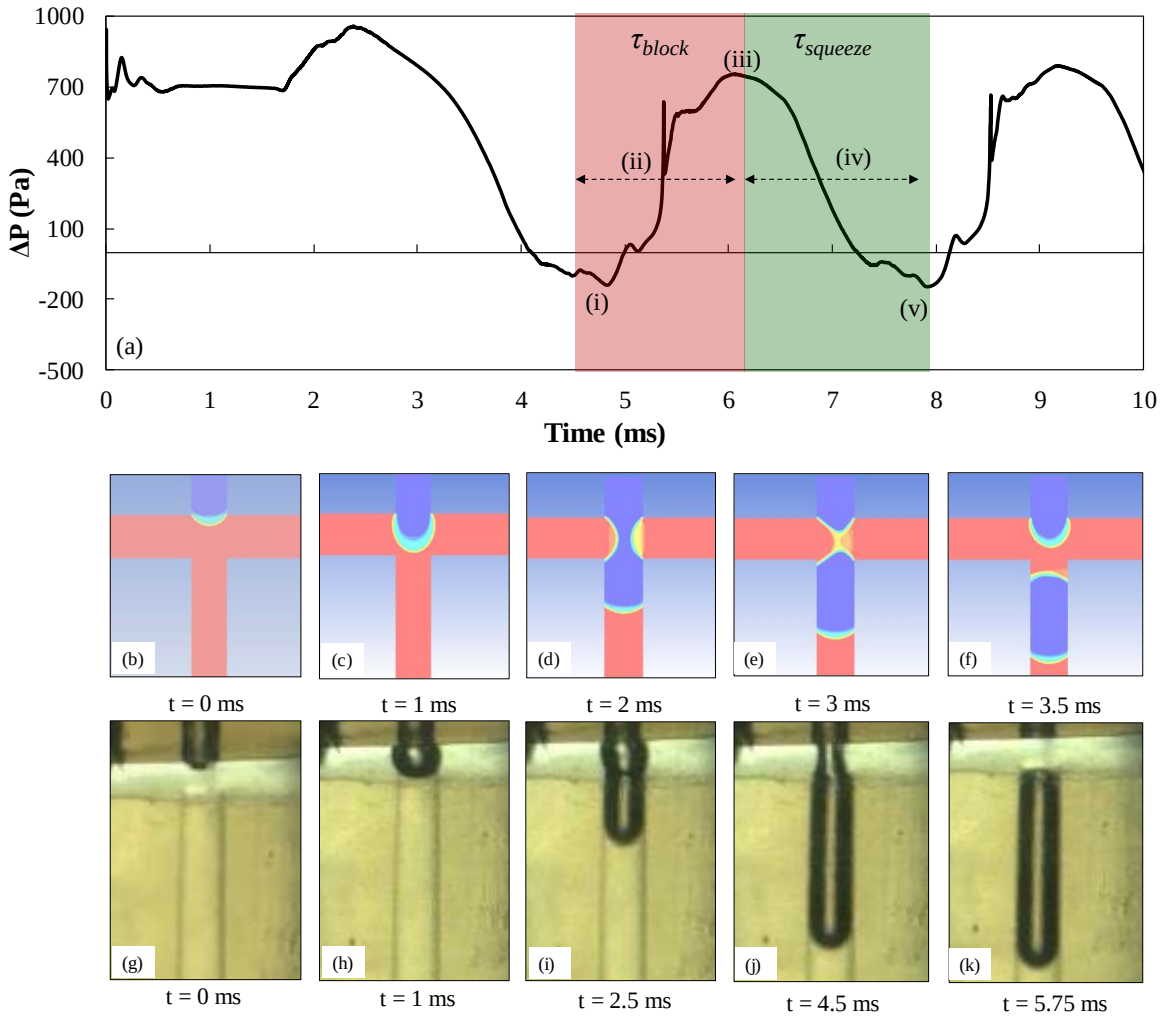

Figure 7. (a) Pressure drop (ΔP) between gas and liquid inlets. Snapshots of microbubble formation (b-f) CFD Simulation (g-k) Experiment for gas velocity of 0.14 m/s and liquid velocity 0.053 m/s.

experimental microbubble formation process (Video S2) for v_g = 0.049 m/s and v_l = 0.159 m/s is presented in Fig. 4 (a-j). The gas interface progressively expands through the mixing zone to the vertical channel and obstructs the liquid stream continuously. The liquid from both ends of the mixing zone constricts the gas phase to generate a neck that eventually thins and pinches off. In this case, v_g / v_l = 0.29, the RHS velocity (v_{rh}) of 0.045 m/s is almost twice as high as the RHS velocity for the gas/liquid velocity ratio v (v_g / v_l) = 1. This finding clearly suggests that a high liquid flow velocity directly affects the RHS velocity during microbubble pinch-off.

Fig. 5 (a- j) showcases snapshots of the simulated and experimental microbubble formation process (Video S3) for v_g=0.027 m/s, v_l=0.053 m/s, and v_{rh} = 0.025 m/s. Similarly, Fig. 6 (a-f) and Fig. 6 (g-l) displays snapshots for the simulated and experimental bubble formation sequence for v_g=0.049 m/s, v_l=0.079 m/s, v_{rh} = 0.03 m/s (Video S4) and v_g=0.067 m/s, v_l=0.053 m/s, and v_{rh} = 0.025 m/s (Video S5), respectively. Experiment and numerical results indicate that the size of the gas slug is higher for high gas to liquid velocity ratios. The process of microbubble pinch-off is consistent across different situations with varying gas-to-liquid velocity ratios. Each microbubble is formed when a stream of gas phase crosses the junction and is squeezed by liquid from both sides at the mixing zone.[58]

Fig. 5-6 and 7(b-k) demonstrates that an increase in gas phase velocity, corresponding to higher gas to liquid velocity ratios, results in a shorter cycle and a higher production rate of microbubble formation. However, this also promotes the generation of large bubbles, as the gas stream elongates further downstream at a constant liquid velocity, as shown in Fig. 5 and 6. In contrast, a higher liquid phase velocity, corresponding to lower gas to liquid velocity ratios, results in a thicker liquid film enveloping the gas phase during pinch-off, as illustrated in Fig. 5. The thicker liquid layer at higher velocities prevents the gas thread from filling the entire cross section, causing quicker and more rapid pinch-off than at lower liquid velocities. The total time for microbubble pinch-off for a velocity ratio (v = 1) is ~ 7 millisecond (ms) (Fig. 3), whereas the total time for a velocity ratio (v = 0.31) is ~ 4.5 ms (Fig. 4). The simulation findings indicate that a decrease in velocity ratio (which corresponds to increase in liquid velocity) results in a decrease in the total time required for each cycle which leads to an higher production rates of microbubbles [27]. Similarly, the total time for v = 0.51 is ~ 7 ms (Fig. 5), and the total time for microbubble formation for v = 2.64 is ~ 3.5 ms (Fig. 7 b-k). As a result, the simulation findings indicate that an increase in velocity ratio

(which corresponds to increase in gas velocity) results in a decrease in the total time required for microbubble formation, but results in large bubble generation due to high gas velocity.

Variation in pressure drop during microbubble formation: Fig. 7A depicts the change in pressure drop for a system and the corresponding snapshots of the High-speed video (Video S6) and simulations for gas-to-liquid velocity ratio of $v_g / v_l = 2.64$ (Fig. 7 b-f & Fig. 7 g-k). The pressure drop is the difference between the average pressure at the liquid inlet and the average pressure at the gas inlet, which can be found at locations 1 and 3 in Fig. 2A. It can be observed that as the gas phase breakup occurs, a new bubble forms, causing the pressure difference to reach a minimum value (stage i). The pressure drop then steadily increases as the gas tip advances and a neck develops (stage i-ii). In stages ii and iii, the gas stream expands in the outflow channel while the liquid phase squeezes the gas phase. Due to the flow restriction, the continuous phase is restricted to extremely narrow layers near the walls of the micro-capillary. These thin films of fluid experience higher flow resistance, leading to the accumulation of pressure in the continuous phase upstream of the tip [59]. Therefore, as the pressure builds-up, the continuous fluid displaces the interface and squeezes the neck of the inner fluid, leading to the formation and eventual separation of a bubble. At stage (iv), the pressure drop decreases rapidly and reaches to a minimum, stage (v), and the entire process is repeated periodically. In other words, the pressure drop rises until the channel is blocked. The time interval for phase (i-iii) is called the blocking time τ_{block} while that of stage (iii-v) is defined as squeezing time $\tau_{squeeze}$.[58] The total time is the summation of the blocking and the squeezing time ($\tau = \tau_{block} + \tau_{squeeze}$). Fig. S3 presents the pressure drop variation owing to differences in the input velocities of the gas phase. It can be observed that the cycle from bubble start to end is similar to alternate crest and troughs. The steady buildup of pressure in the continuous phase upstream was found to grow proportionally with the increase in gas phase

velocity. Fig. S3 also shows that increasing the velocity ratio enhances the frequency of the crest and trough formed during microbubble pinch off. This demonstrates that increasing the gas velocity causes an increase in the pressure buildup in the upstream liquid phase. Since this buildup pressure is larger than the pressure at the immiscible tip, the continuous liquid phase squeezes the gas stream at a faster rate to create a neck, hence enhancing the production rate of microbubbles.

Velocity distribution during microbubble formation: Figures 8 depict velocity vectors for various gas and liquid flow rates, illustrating flow phenomena surrounding the gas slug. The velocity vectors and volume fraction are superimposed to show how the magnitude of the velocity vector varies during microbubble formation. Figures 8 (a-d) presents the velocity vector for microbubble generation for v_l =0.053 m/s and v_g = 0.027 m/s. The microbubble formation is divided into two phases (i) the blocking period (Fig. 8a and b) and the squeezing period (Fig. 8c-d). During the blocking period, the gas phase occupies most of the junction volume, leaving little space for the liquid to proceed towards the exit channel. Due to the reduction in cross-sectional area for the same intake volumetric flow rate, the obstruction causes an increase in local velocities around the partly formed gas bubble. As the gas slug evolves at the junction (Figure 8b), the rise in local velocity sets the inception of the neck formation and begins the squeezing period. The commencement of the squeezing phase is reflected by the formation of a neck when pressure forces begin to exceed surface tension forces. Figure 8c depicts the situation after the neck has been produced and the gas thread has shrunk by ~50% of its original size. It can be observed that the liquid is prevented from moving downward and instead attempts to move upward into the neck region, causing recirculations at the upper and lower corners. Maximum liquid velocities were observed to be three times greater than inlet velocities, indicating the influence of larger pressure drop during microbubble generation. Larger local velocities are caused by a low-pressure zone or

a larger pressure drop near the junction (as mentioned in "Variation in pressure drop during microbubble formation" section). Recirculations were also seen at the corners of the junction, which may have been generated by flow disruptions brought on by neck formation and pinch-off. Three distinct recirculation zones after microbubble pinch off can be observed (Fig. 8d), two at the top and one at the bottom near the corners possibly because the local liquid from both horizontal channel rushes into the low pressure zone created due to pinch off.

Fig. 8 (e-h) depicts the velocity distribution for the liquid velocity (v_l) of 0.053 m/s and the gas velocity (v_g) of 0.049 m/s. Interestingly, as the gas evolves near the junction, counter-rotating vortices located at the upper corners of the gas phase are observed to be formed, as depicted in Fig. 8e (magnified section). The formation of vortices suggests that prior to the initiation of neck formation, the gas velocities within the gas slug located at the corners of the neck generate counter-rotating vortices, resulting in the formation of low-pressure zones that possibly facilitate neck formation. Upon a subsequent reduction in the cross-sectional area required for fluid flow, there is a notable increase in the velocities of the liquid, as evidenced by the observations presented in Fig. 8 (e-h). The remaining phenomena exhibit similarities to the previously described case.

Fig. 8(i – l) displays the velocity distributions corresponding to v_l = 0.053 m/s and v_g = 0.140 m/s. Similar to the previous case, a region of reduced pressure is formed as a result of the decreased cross-sectional area. The reduction in cross-sectional area leads to an increase in the velocity of the liquid flowing through the lower section and exiting through the outlet, as depicted in Figure 8j.

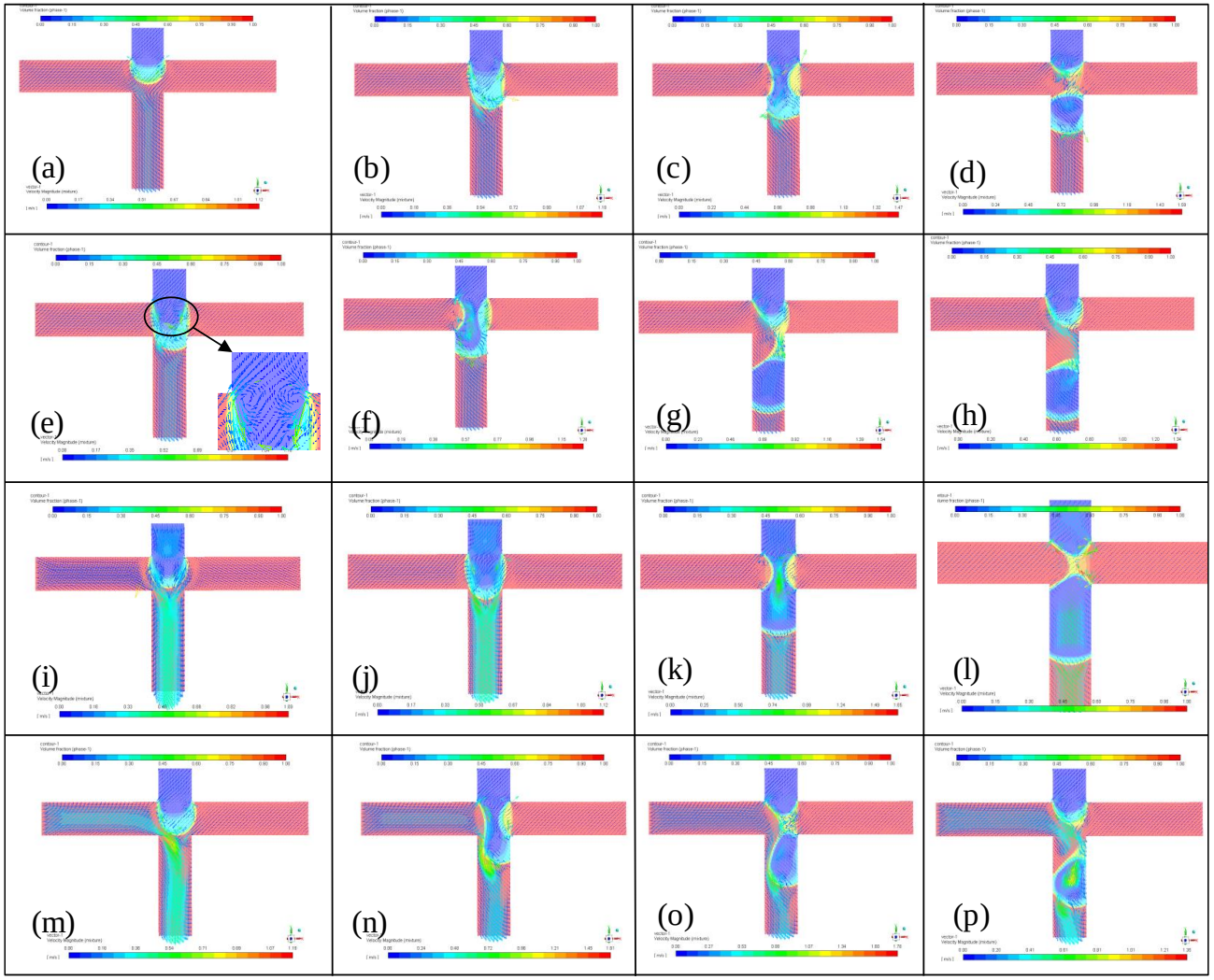

Figure 8. Velocity vector superimposed with volume fraction. (a-d) v_l = 0.053 m/s; v_g = 0.027 m/s; (e-h) v_l = 0.053 m/s; v_g = 0.049 m/s; (i-l) v_l = 0.053 m/s; v_g = 0.14 m/s; (m-p) v_l = 0.159 m/s; v_g = 0.049 m/s

The decrease in pressure gradient observed during neck formation exhibit similarities to those elucidated in the preceding scenario. During the process of pinch-off, it was observed that the velocities of the liquid in the immediate vicinity of the neck region are significantly higher, as depicted in Figure 8k. Conversely, once the bubble has fully formed, the surrounding fluid rapidly fills the previously gas-filled region, exhibiting recirculation, as illustrated in Fig. 8l.

Figures 8 (m-p) depicts the velocity distribution for the liquid velocity (v_l) of 0.159 m/s and the gas velocity (v_g) of 0.049 m/s. In contrast to prior instances, when the liquid phase velocity is high, we observed a distinct separation between the wall and the interface of the gas-liquid (GL) near the left wall. High liquid phase velocity demonstrates a significant fluctuation in the blocking and squeezing duration during microbubble formation. The presence of elevated liquid velocities in the vicinity, results in the gas-liquid interface being incapable of establishing contact with the left wall, as illustrated in Figs. 8n and 8o. Due to the subsequent obstruction of the flow channel by the gas-phase, the local velocity at the mixing zone rise at least three to four times higher than the velocities of the liquid entering the system. Increased liquid phase velocities were observed to lead to faster microbubble pinch-off, possibly due to elevated shear force and squeezing pressure[60]. The formation of microbubbles is still considered to follow a squeezing phase, as the gas phase continues to occupy the majority of the junction volume. Higher liquid velocities were observed to produces lower size of microbubbles compared to previous cases.

Effect of liquid and gas velocity on production rates, microbubble size, and RHS velocity: Fig. 9 (a-c) depicts the change in production rate, microbubble size and RHS velocity when the liquid velocity is increased at a constant gas velocity. Fig. 9 (d-g) present the optical micrographs for liquid velocity of 0.027 m/s, 0.079 m/s, 0.103 m/s, 0.159 m/s, respectively. It can be observed from Fig. 9a that for both experiments and simulations an increase in liquid velocity leads to an

increase in the production rate of microbubbles. A good agreement is observed between simulations and experimental data, with a variance of ~ 15%. The change in microbubble size (Fig. 9b) can be observed to demonstrate a linear decrease in bubble size with the increase in liquid velocity. The decrease in microbubble size was also evident from the optical images of microbubbles captured at the various liquid velocities (Fig. 9 d-g). Moreover, the experimental and simulated microbubble size was observed to match closely, with a variance of ~10%.

Experimental data show a steady increase in the production rate as gas velocity increases (Fig. 10 a). The CFD simulation findings for the production rate (bubbles/sec) match the experimental results with a 12 - 20% coefficient of variance. The increase in microbubble size with the increase in gas velocity was observed to yield a comparable consistency between experimental and simulated results (Fig. 10b). The increase in microbubble size was also evident from the optical images of microbubbles captured at the various gas velocities (Fig. 10 d-g). The deviation is simulation result is attributed to the back flow (RHS) velocity introduced for bubble formation. For determination of RHS velocity, first a single phase simulation with liquid flow from one inlet and a wall on the other end of the T-junction were performed and the back flow velocity was noted. The backflow velocity at the T-junction was noted and used as RHS velocity for gas-liquid two-phase simulations. Inspite of a comprehensive procedure to arrive at RHS velocity the inherent challenge to mimic real scenario is responsible for higher deviations in some cases.

Fig. 9c presents the change in RHS velocity when the liquid velocity was increased from 0.027 m/s to 0.159 m/s while the gas velocity was held constant at 0.049 m/s. The RHS velocity was nearly constant at 0.025 m/s at lower liquid velocities from 0.027 to 0.05 m/s, resulting in a flat curve. However, the RHS velocity increases upto ~ 0.042 m/s with the increase in liquid velocity from 0.05 m/s to 0.13 m/s.

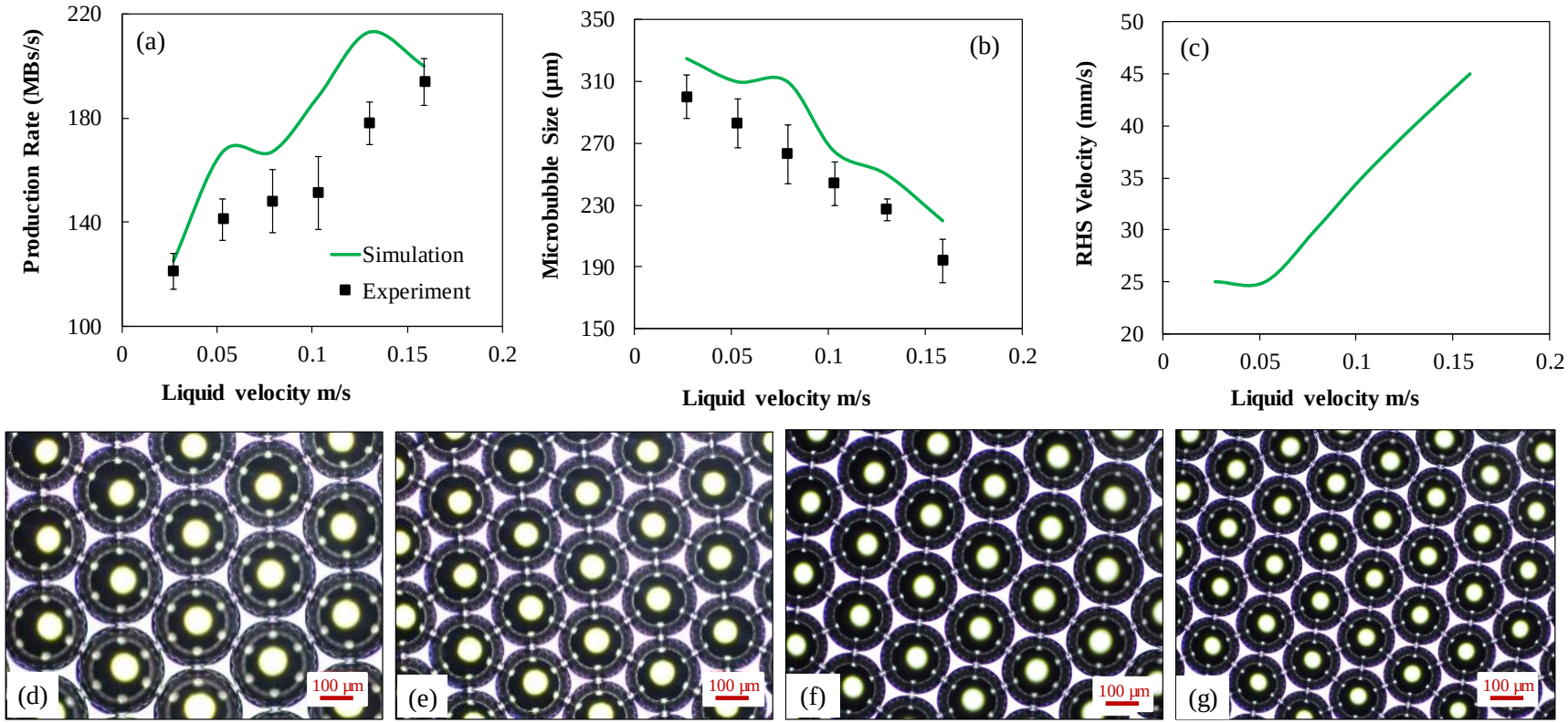

Figure 9. Bubble characteristics for gas-liquid flow in T-junction microfluidic device (a) Variation in production rate (Microbubbles (MBs)/s) with change in liquid velocity (b) Variation in microbubble size with change in liquid velocity (c) Change in RHS velocity when liquid velocity increases from 0.027 m/s to 0.159 m/s at constant gas velocity of 0.049 m/s (d-g) Optical images of microbubbles for liquid velocity of 0.027 m/s, 0.079 m/s, 0.103 m/s, and 0.159 m/s, respectively at constant gas velocity of 0.049 m/s. Black markers represent experimental data and smooth line represent simulation.

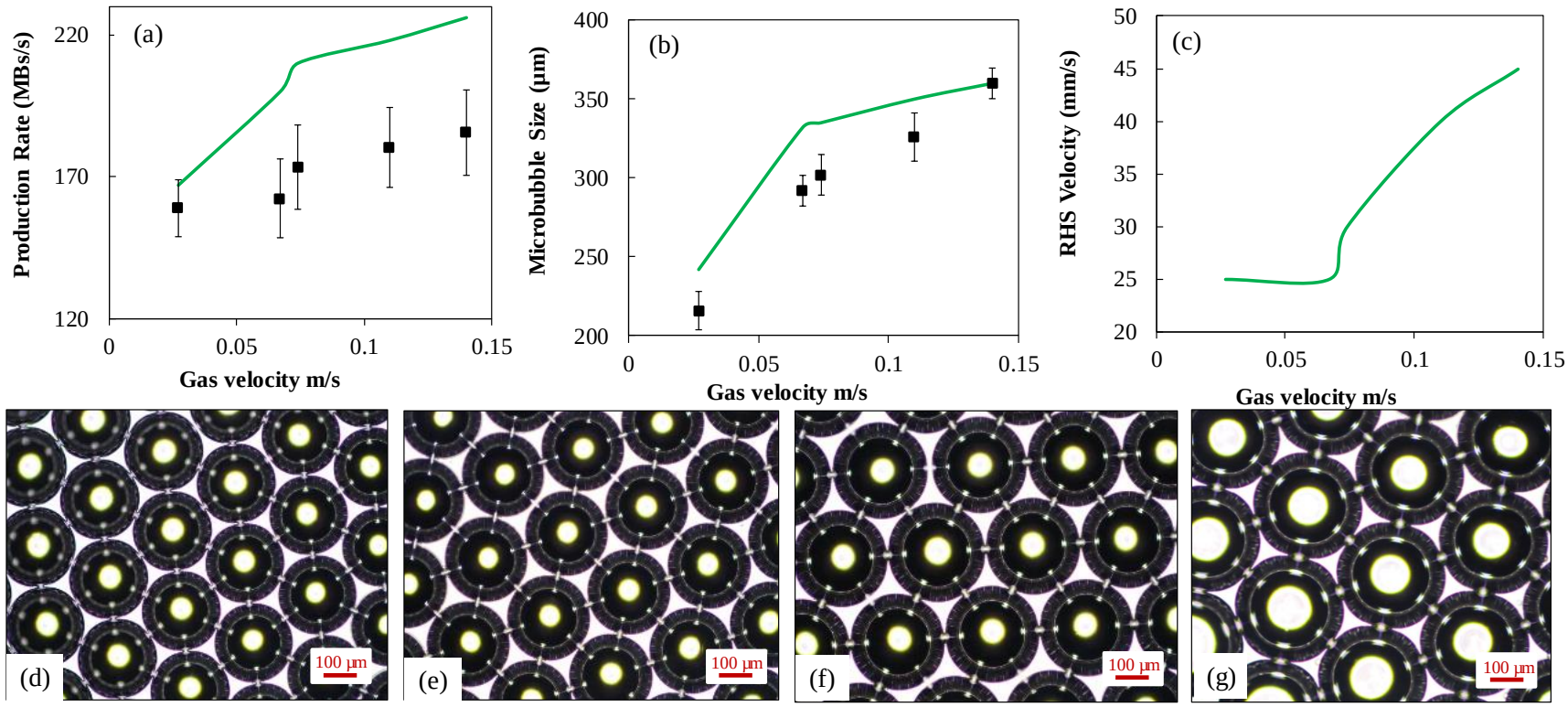

Figure 10. Bubble characteristics for gas-liquid flow in T-junction microfluidic device (a) Variation in production rate with change in gas velocity (b) Variation in microbubble size with change in gas velocity (c) Change in RHS velocity when the gas velocity increases from 0.027 m/s to 0.14 m/s at constant liquid velocity of 0.053 m/s. (d-g) Optical images of microbubbles for gas velocity of 0.027 m/s, 0.067 m/s, 0.11 m/s, and 0.14 m/s, respectively at constant liquid velocity of 0.053 m/s. Black markers represent experimental data and smooth line represent simulation.

The inlet velocity of the liquid phase directly influences the RHS velocity. Due to a greater incoming liquid velocity, more liquid is filled up near the mixing zone; as a consequence, the presence of a wall generates a higher backflow, possibly increasing the RHS velocity. Fig. 10c presents the variation in RHS velocity when the gas velocity was increased from 0.027 m/s to 0.14 m/s while the liquid velocity was held constant at 0.053 m/s. At lower gas velocity from 0.027 m/s to 0.069 m/s the RHS velocity was observed to be nearly constant. However, at higher gas velocities from 0.074 to 0.14 m/s the RHS velocity was observed to rise upto 0.045 m/s. This demonstrates that the RHS velocity has a strong dependency on the flow velocities of the liquid and gas phases.

Comparison of microbubble formation in CETM devices with back flow and conventional T-junction without back flow.

As discussed in the previous sections, the current investigation focuses on a T-junction configuration that involves a mixing region where the liquid phase experiences a back flow during microbubble formation. The occurrence of backflow observed during the microbubble formation has been observed to aid microbubble generation by accelerating the pinch-off of gas slugs. To understand the role of mixing zone on microbubble formation further, we conducted simulations for conventional T-junction with specific fluid flow velocities while ensuring the absence of backflow. A single horizontal channel for a liquid inlet, and a vertical channel for gas inlet was modelled to conduct the study. Two distinct scenarios were simulated (i) v_l = 0.159 m/s and v_g = 0.49 m/s, (ii) v_l = 0.53 m/s and v_g = 0.14 m/s. Interestingly, we observed that the numerical domain used for simulating CETM devices with back flow was inadequate to accurately simulate the formation of bubbles in conventional T-junction devices. Therefore, a domain of greater size was selected to simulate the microbubble in conventional T-junction devices where the length of the

top limb was three times, and the bottom limb was four times longer than the length of the initial bottom limb used for simulation of CETM devices. Fig. S4 presents the volume fraction contours for (i) v_l = 0.159 m/s and v_g = 0.49 m/s, (ii) v_l = 0.53 m/s and v_g = 0.14 m/s, respectively. It is evident from fig. S4 that the sizes of the gas slug generated by conventional devices are comparatively larger than those produced by CETM devices under similar flow conditions. The production rates of microbubble formation with backflow were estimated to be 18% and 24% higher in case (i) and (ii), respectively, compared to microbubble formation without backflow. Moreover, The location of the microbubble pinch-off for vl = 0.159 m/s and vg = 0.49 m/s was found to be farther downstream compared to CETM devices, suggesting a shift in microbubble production regime at higher liquid velocities[60]. The phenomenon of bubble pinch-off in conventional T-junctions displayed resemblances to previous studies[60]. The large size of the microbubbles in conventional devices compared to CETM devices suggests that the presence of back flow in CETM devices exerts additional shear force for pinch-off of gas slug during microbubble formation. Therefore, the smaller size of microbubbles and their rapid pinch-off indicate that the occurrence of backflow during microbubble formation enhances the process of microbubble formation.

Conclusions

In this study, we utilize experimental and computational methods (computational fluid dynamics) to examine the microbubble formation process in a T-junction microfluidic device. CFD simulation were performed using volume of fluid (VOF) approach using ANSYS Fluent. The fluid phases consisted of (i) aqueous suspension of Bovine serum albumin (BSA) as the liquid phase and (ii) nitrogen gas (N_2) as the gas phase. The operational parameters, such as the gas and liquid phase velocities, were varied to determine their influence on microbubble formation.

Experiments demonstrated that the size of microbubbles decreased with the increase in liquid phase velocity while keeping the gas velocity constant. On the other hand, when the gas velocity increased while keeping the liquid velocity constant, a sharp rise in bubble size was observed up to 0.074 m/s, after which the bubble size became nearly constant. In both simulations and experiments, the production rate of microbubbles increased as the velocity of the liquid and/or gas increased, while keeping the velocity of the gas and liquid constant, respectively. Additionally, an increase in the velocity ratio at a constant velocity of the liquid phase decreased the total time required for a single microbubble pinch-off. The decrement in total time necessary for pinch-off was evident from the pressure versus time plots, which revealed that an increase in velocity ratio caused a rise in microbubble pinch-off frequency. The pressure build-up in the continuous phase upstream was observed to grow proportionately to the velocity of the gas phase. Therefore, a more significant pressure build-up at the upstream continuous liquid phase at higher gas velocity compressed and constricted the gas stream faster to produce a neck, thereby increasing the rate of microbubble production.

Our findings indicate that operational parameters such as gas and liquid velocities and the velocity ratio play a significant role in bubble formation in microfluidic devices. These insights will allow improvement in size reduction of microbubbles for various applications, such as drug delivery and medical diagnostics.

Supplementary Information

High-speed video of microbubble formation in T-junction device for v_g = 0.049 & v_l = 0.053 (Video S1), v_g = 0.049 & v_l = 0.159 (Video S2), v_g = 0.027 & v_l = 0.053 (Video S3), v_g = 0.049 & v_l = 0.079 (Video S4), v_g = 0.067 & v_l = 0.053 (Video S5), v_g = 0.14 & v_l = 0.053 (Video S6).

Acknowledgements: The authors gratefully acknowledge the funding from UGC-UKIERI Joint Research Programme (UKIERI III) through a grant no. 184-7/2018 (IC). The authors acknowledge the mechanical workshop facility at UCL, high performance computational facility at IIT Gandhinagar and computation facility at Ahmedabad University to carry out this work. The authors also acknowledge the financial support from Ministry of Education (MoE), Government of India.

References

1. Upadhyay, A.; Dalvi, S. V., Synthesis, characterization and stability of BSA-encapsulated microbubbles. *RSC Advances* **2016,** *6* (18), 15016-15026.
2. Navarro-Becerra, J. A.; Song, K.-H.; Martinez, P.; Borden, M. A., Microbubble Size and Dose Effects on Pharmacokinetics. *ACS Biomaterials Science & Engineering* **2022,** *8* (4), 1686-1695.
3. Segers, T.; De Rond, L.; De Jong, N.; Borden, M.; Versluis, M., Stability of monodisperse phospholipid-coated microbubbles formed by flow-focusing at high production rates. *Langmuir* **2016,** *32* (16), 3937-3944.
4. Ferrara, K.; Pollard, R.; Borden, M., Ultrasound microbubble contrast agents: fundamentals and application to gene and drug delivery. *Annu. Rev. Biomed. Eng.* **2007,** *9*, 415-447.
5. Schoen Jr, S.; Kilinc, M. S.; Lee, H.; Guo, Y.; Degertekin, F. L.; Woodworth, G. F.; Arvanitis, C., Towards controlled drug delivery in brain tumors with microbubble-enhanced focused ultrasound. *Advanced Drug Delivery Reviews* **2022,** *180*, 114043.
6. Nawijn, C.; Segers, T.; Lajoinie, G.; Mørch, Ý.; Berg, S.; Snipstad, S.; de Lange Davies, C.; Versluis, M., Multi-timescale microscopy methods for the characterization of fluorescently-labeled microbubbles for ultrasound-triggered drug release. *JoVE (Journal of Visualized Experiments)* **2021,** (172), e62251.
7. Omata, D.; Munakata, L.; Kageyama, S.; Suzuki, Y.; Maruyama, T.; Shima, T.; Chikaarashi, T.; Kajita, N.; Masuda, K.; Tsuchiya, N., Ultrasound image-guided gene delivery using three-dimensional diagnostic ultrasound and lipid-based microbubbles. *Journal of Drug Targeting* **2022,** *30* (2), 200-207.
8. Upadhyay, A.; Dalvi, S. V., Microbubble formulations: synthesis, stability, modeling and biomedical applications. *Ultrasound in medicine & biology* **2019,** *45* (2), 301-343.
9. Langeveld, S. A.; Meijlink, B.; Kooiman, K., Phospholipid-coated targeted microbubbles for ultrasound molecular imaging and therapy. *Current Opinion in Chemical Biology* **2021,** *63*, 171-179.
10. Helbert, A.; Gaud, E.; Segers, T.; Botteron, C.; Frinking, P.; Jeannot, V., Monodisperse versus Polydisperse Ultrasound Contrast Agents: In Vivo Sensitivity and safety in Rat and Pig. *Ultrasound in Medicine & Biology* **2020,** *46* (12), 3339-3352.
11. Pancholi, K.; Stride, E.; Edirisinghe, M., Generation of microbubbles for diagnostic and therapeutic applications using a novel device. *Journal of drug targeting* **2008,** *16* (6), 494-501.
12. Segers, T.; Lohse, D.; Versluis, M.; Frinking, P., Universal equations for the coalescence probability and long-term size stability of phospholipid-coated Monodisperse microbubbles formed by flow focusing. *Langmuir* **2017,** *33* (39), 10329-10339.
13. Khan, A. H.; Jiang, X.; Kaushik, A.; Nair, H. S.; Edirisinghe, M.; Mercado-Shekhar, K. P.; Shekhar, H.; Dalvi, S. V., Combining Ultrasound and Capillary-Embedded T-Junction Microfluidic Devices

to Scale Up the Production of Narrow-Sized Microbubbles through Acoustic Fragmentation. *Langmuir* **2022,** *38* (33), 10288-10304.
14. Shih, R.; Bardin, D.; Martz, T. D.; Sheeran, P. S.; Dayton, P. A.; Lee, A. P., Flow-focusing regimes for accelerated production of monodisperse drug-loadable microbubbles toward clinical-scale applications. *Lab on a Chip* **2013,** *13* (24), 4816-4826.
15. Soysal, U.; Azevedo, P. N.; Bureau, F.; Aubry, A.; Carvalho, M. S.; Pessoa, A. C.; Lucimara, G.; Couture, O.; Tourin, A.; Fink, M., Freeze-dried microfluidic monodisperse microbubbles as a new generation of ultrasound contrast agents. *Ultrasound in Medicine & Biology* **2022,** *48* (8), 1484-1495.
16. Castro-Hernandez, E.; Van Hoeve, W.; Lohse, D.; Gordillo, J. M., Microbubble generation in a co-flow device operated in a new regime. *Lab on a Chip* **2011,** *11* (12), 2023-2029.
17. Kang, K.-K.; Lee, B.; Lee, C.-S., Microfluidic approaches for the design of functional materials. *Microelectronic Engineering* **2018,** *199*, 1-15.
18. Khan, A. H.; Jiang, X.; Surwase, S.; Gultekinoglu, M.; Bayram, C.; Sathisaran, I.; Bhatia, D.; Ahmed, J.; Wu, B.; Ulubayram, K., Effectiveness of oil-layered albumin microbubbles produced using microfluidic T-junctions in series for in vitro inhibition of tumor cells. *Langmuir* **2020,** *36* (39), 11429-11441.
19. Pulsipher, K. W.; Hammer, D. A.; Lee, D.; Sehgal, C. M., Engineering theranostic microbubbles using microfluidics for ultrasound imaging and therapy: a review. *Ultrasound in medicine & biology* **2018,** *44* (12), 2441-2460.
20. Garstecki, P.; Gitlin, I.; DiLuzio, W.; Whitesides, G. M.; Kumacheva, E.; Stone, H. A., Formation of monodisperse bubbles in a microfluidic flow-focusing device. *Applied Physics Letters* **2004,** *85* (13), 2649-2651.
21. Utada, A. S.; Fernandez-Nieves, A.; Stone, H. A.; Weitz, D. A., Dripping to jetting transitions in coflowing liquid streams. *Physical review letters* **2007,** *99* (9), 094502.
22. Baroud, C. N.; Gallaire, F.; Dangla, R., Dynamics of microfluidic droplets. *Lab on a Chip* **2010,** *10* (16), 2032-2045.
23. Garstecki, P.; Fuerstman, M. J.; Stone, H. A.; Whitesides, G. M., Formation of droplets and bubbles in a microfluidic T-junction—scaling and mechanism of break-up. *Lab on a Chip* **2006,** *6* (3), 437-446.
24. Zhang, Y.; Wang, L., Experimental investigation of bubble formation in a microfluidic T-shaped junction. *Nanoscale and Microscale Thermophysical Engineering* **2009,** *13* (4), 228-242.
25. Parhizkar, M.; Edirisinghe, M.; Stride, E., Effect of operating conditions and liquid physical properties on the size of monodisperse microbubbles produced in a capillary embedded T-junction device. *Microfluidics and nanofluidics* **2013,** *14* (5), 797-808.
26. Parhizkar, M.; Edirisinghe, M.; Stride, E., The effect of surfactant type and concentration on the size and stability of microbubbles produced in a capillary embedded T-junction device. *Rsc Advances* **2015,** *5* (14), 10751-10762.
27. Jiang, X.; Zhang, Y.; Edirisinghe, M.; Parhizkar, M., Combining microfluidic devices with coarse capillaries to reduce the size of monodisperse microbubbles. *RSC advances* **2016,** *6* (68), 63568-63577.
28. Khan, A. H.; Surwase, S.; Jiang, X.; Edirisinghe, M.; Dalvi, S. V., Enhancing in vitro stability of Albumin Microbubbles produced using Microfluidic T-Junction device. *Langmuir* **2021,** *38* (17), 5052-5062.
29. Pancholi, K.; Stride, E.; Edirisinghe, M., Dynamics of bubble formation in highly viscous liquids. *Langmuir* **2008,** *24* (8), 4388-4393.
30. Parhizkar, M.; Stride, E.; Edirisinghe, M., Preparation of monodisperse microbubbles using an integrated embedded capillary T-junction with electrohydrodynamic focusing. *Lab on a Chip* **2014,** *14* (14), 2437-2446.

31. Bayram, C.; Jiang, X.; Gultekinoglu, M.; Ozturk, S.; Ulubayram, K.; Edirisinghe, M., Biofabrication of Gelatin Tissue Scaffolds with Uniform Pore Size via Microbubble Assembly. *Macromolecular Materials and Engineering* **2019,** *304* (11), 1900394.
32. Katsakouli, C.; Jiang, X.; Lau, W. K.; Rohn, J. L.; Edirisinghe, M., Generating Antibacterial Microporous Structures Using Microfluidic Processing. *ACS Omega* **2019,** *4* (1), 2225-2233.
33. Wu, B.; Luo, C.; Palaniappan, A.; Jiang, X.; Gultekinoglu, M.; Ulubayram, K.; Bayram, C.; Harker, A.; Shirahata, N.; Khan, A. H., Generating lifetime-enhanced microbubbles by decorating shells with silicon quantum nano-dots using a 3-series T-junction microfluidic device. *Langmuir* **2022,** *38* (36), 10917-10933.
34. Cleve, S.; Diddens, C.; Segers, T.; Lajoinie, G.; Versluis, M., Time-resolved velocity and pressure field quantification in a flow-focusing device for ultrafast microbubble production. *Physical review fluids* **2021,** *6* (11), 114202.
35. van Steijn, V.; Kreutzer, M. T.; Kleijn, C. R., μ-PIV study of the formation of segmented flow in microfluidic T-junctions. *Chemical Engineering Science* **2007,** *62* (24), 7505-7514.
36. Abate, A. R.; Mary, P.; van Steijn, V.; Weitz, D. A., Experimental validation of plugging during drop formation in a T-junction. *Lab on a Chip* **2012,** *12* (8), 1516-1521.
37. Romero, P. A.; Abate, A. R., Flow focusing geometry generates droplets through a plug and squeeze mechanism. *Lab on a Chip* **2012,** *12* (24), 5130-5132.
38. Jia, H.; Zhang, P., Bubble formation in viscous fluids by a microfluidic flow-focusing junction: A computational study. *Microfluidics and Nanofluidics* **2020,** *24* (11), 1-16.
39. Santos, R. M.; Kawaji, M., Numerical modeling and experimental investigation of gas–liquid slug formation in a microchannel T-junction. *International Journal of Multiphase Flow* **2010,** *36* (4), 314-323.
40. Wu, Y.; Fu, T.; Zhu, C.; Ma, Y.; Li, H. Z., Bubble coalescence at a microfluidic T-junction convergence: from colliding to squeezing. *Microfluidics and nanofluidics* **2014,** *16*, 275-286.
41. Nagrath, S.; Jansen, K. E.; Lahey Jr, R. T., Computation of incompressible bubble dynamics with a stabilized finite element level set method. *Computer Methods in Applied Mechanics and Engineering* **2005,** *194* (42-44), 4565-4587.
42. Nichita, B. A.; Zun, I.; Thome, J. R., A level set method coupled with a volume of fluid method for modeling of gas-liquid interface in bubbly flow. *Journal of fluids engineering* **2010,** *132* (8).
43. Akbar, M.; Ghiaasiaan, S., Simulation of Taylor flow in capillaries based on the volume-of-fluid technique. *Industrial & engineering chemistry research* **2006,** *45* (15), 5396-5403.
44. De Schepper, S. C.; Heynderickx, G. J.; Marin, G. B., CFD modeling of all gas–liquid and vapor–liquid flow regimes predicted by the Baker chart. *Chemical Engineering Journal* **2008,** *138* (1-3), 349-357.
45. Gupta, R.; Fletcher, D. F.; Haynes, B. S., On the CFD modelling of Taylor flow in microchannels. *Chemical Engineering Science* **2009,** *64* (12), 2941-2950.
46. Hirt, C. W.; Nichols, B. D., Volume of fluid (VOF) method for the dynamics of free boundaries. *Journal of computational physics* **1981,** *39* (1), 201-225.
47. Liu, X.; Zhang, C.; Yu, W.; Deng, Z.; Chen, Y., Bubble breakup in a microfluidic T-junction. *Science Bulletin* **2016,** *61* (10), 811-824.
48. Pham, H.; Wen, L.; Zhang, H., Numerical simulation and analysis of gas-liquid flow in a T-junction microchannel. *Advances in Mechanical Engineering* **2012,** *4*, 231675.
49. Arias, S.; Montlaur, A., Numerical study and experimental comparison of two-phase flow generation in a T-junction. *AIAA journal* **2017,** *55* (5), 1565-1574.
50. Chang, J.; Cai, J., Numerical research on bubble formation process in microchannel using diffuse Interface method. *Heat and Mass Transfer* **2019,** *55* (11), 3133-3149.
51. Fu, T.; Ma, Y.; Funfschilling, D.; Li, H. Z., Bubble formation and breakup mechanism in a microfluidic flow-focusing device. *Chemical Engineering Science* **2009,** *64* (10), 2392-2400.

52. Xiong, R.; Bai, M.; Chung, J. N., Formation of bubbles in a simple co-flowing micro-channel. *Journal of Micromechanics and Microengineering* **2007,** *17* (5), 1002.
53. Brackbill, J. U.; Kothe, D. B.; Zemach, C., A continuum method for modeling surface tension. *Journal of computational physics* **1992,** *100* (2), 335-354.
54. Rider, W. J.; Kothe, D. B., Reconstructing volume tracking. *Journal of computational physics* **1998,** *141* (2), 112-152.
55. Leonard, B. P., A stable and accurate convective modelling procedure based on quadratic upstream interpolation. *Computer methods in applied mechanics and engineering* **1979,** *19* (1), 59-98.
56. Issa, R. I., Solution of the implicitly discretised fluid flow equations by operator-splitting. *Journal of computational physics* **1986,** *62* (1), 40-65.
57. Sun, L.; Fan, M.; Li, P.; Yu, H.; Zhang, Y.; Xu, J.; Jiang, W.; Qian, S.; Sun, G., Microbubble characteristic in a T-junction microchannel in microfluidic chip. *Molecular Physics* **2019,** *117* (18), 2535-2545.
58. De Menech, M.; Garstecki, P.; Jousse, F.; Stone, H. A., Transition from squeezing to dripping in a microfluidic T-shaped junction. *journal of fluid mechanics* **2008,** *595*, 141-161.
59. Garstecki, P.; Stone, H. A.; Whitesides, G. M., Mechanism for flow-rate controlled breakup in confined geometries: A route to monodisperse emulsions. *Physical review letters* **2005,** *94* (16), 164501.
60. Fu, T.; Ma, Y.; Funfschilling, D.; Zhu, C.; Li, H. Z., Squeezing-to-dripping transition for bubble formation in a microfluidic T-junction. *Chemical engineering science* **2010,** *65* (12), 3739-3748.

Table of Contents Use Only

Experimental and Computational Investigation of Microbubble Formation in a Single Capillary Embedded T-junction Microfluidic Device

Aaqib H. Khan[#], Arijit Ganguli[†], Mohan Edirisinghe[‡], and Sameer V. Dalvi[#]*

Chemical Engineering, Indian Institute of Technology Gandhinagar, Palaj, Gandhinagar - 382355, Gujarat, India

† School of Engineering and Applied Sciences, Ahmedabad University, Ahmedabad-380009, Gujarat, India

‡ Department of Mechanical Engineering, University College London (UCL), London WC1E 7JE, U.K.

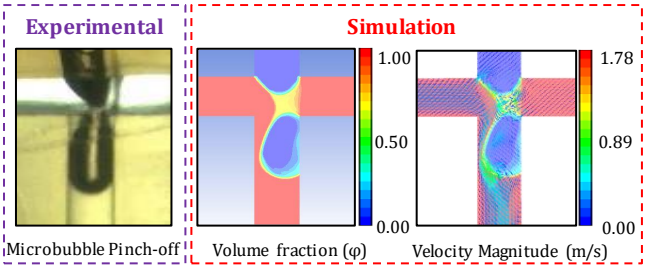

Experimental and Computational Investigation of Microbubble Formation in a single capillary embedded T-junction Microfluidic Device

Aaqib H. Khan[#], Arijit Ganguli[†], Mohan Edirisinghe[‡], and Sameer V. Dalvi[#]*

Chemical Engineering, Indian Institute of Technology Gandhinagar, Palaj, Gandhinagar - 382355, Gujarat, India

† School of Engineering and Applied Sciences, Ahmedabad University, Ahmedabad-380009, Gujarat, India

‡ Department of Mechanical Engineering, University College London (UCL), London WC1E 7JE, U.K.

***E-mail: sameervd@iitgn.ac.in; Phone: 091-79-2395 2408**

Number of pages: 6

Number of figures: 4 (S1, S2, S3, S4)

Caption for the supplementary videos:

High-speed video of microbubble formation in T-junction device for v_g = 0.049 & v_l = 0.053 **(Video S1).**

High-speed video of microbubble formation in T-junction device for v_g = 0.049 & v_l = 0.159 **(Video S2).**

High-speed video of microbubble formation in T-junction device for v_g = 0.027 & v_l = 0.053 **(Video S3).**

High-speed video of microbubble formation in T-junction device for v_g = 0.049 & v_l = 0.079 **(Video S4).**

High-speed video of microbubble formation in T-junction device for v_g = 0.067 & v_l = 0.053 **(Video S5).**

High-speed video of microbubble formation in T-junction device for v_g = 0.14 & v_l = 0.053 **(Video S6).**

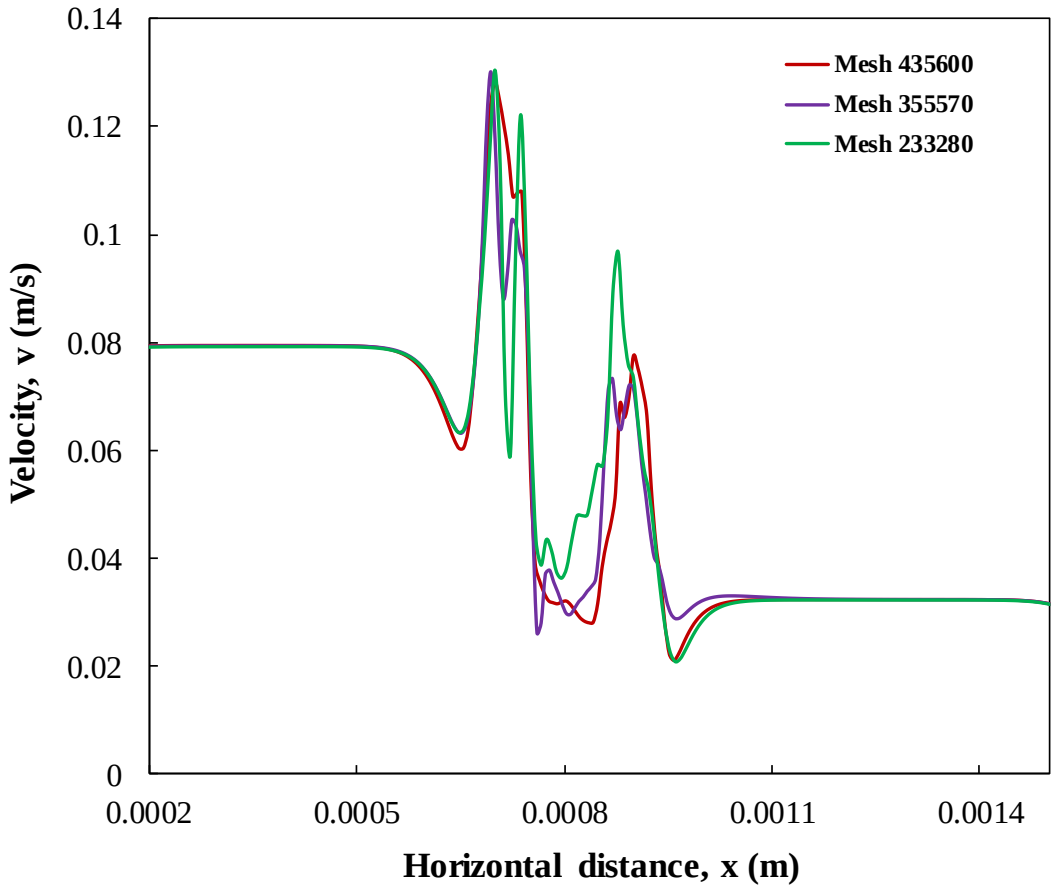

Figure S1. Grid sensitivity for bubble formation during the onset of pinch off (t=0). Grid sensitivity was conducted for three different mesh elements 233280 (coarse), 355570 (medium) and 435600 (fine). The highest deviation for velocity was found to be 27% between coarse and medium mesh and 4 % between medium and fine mesh

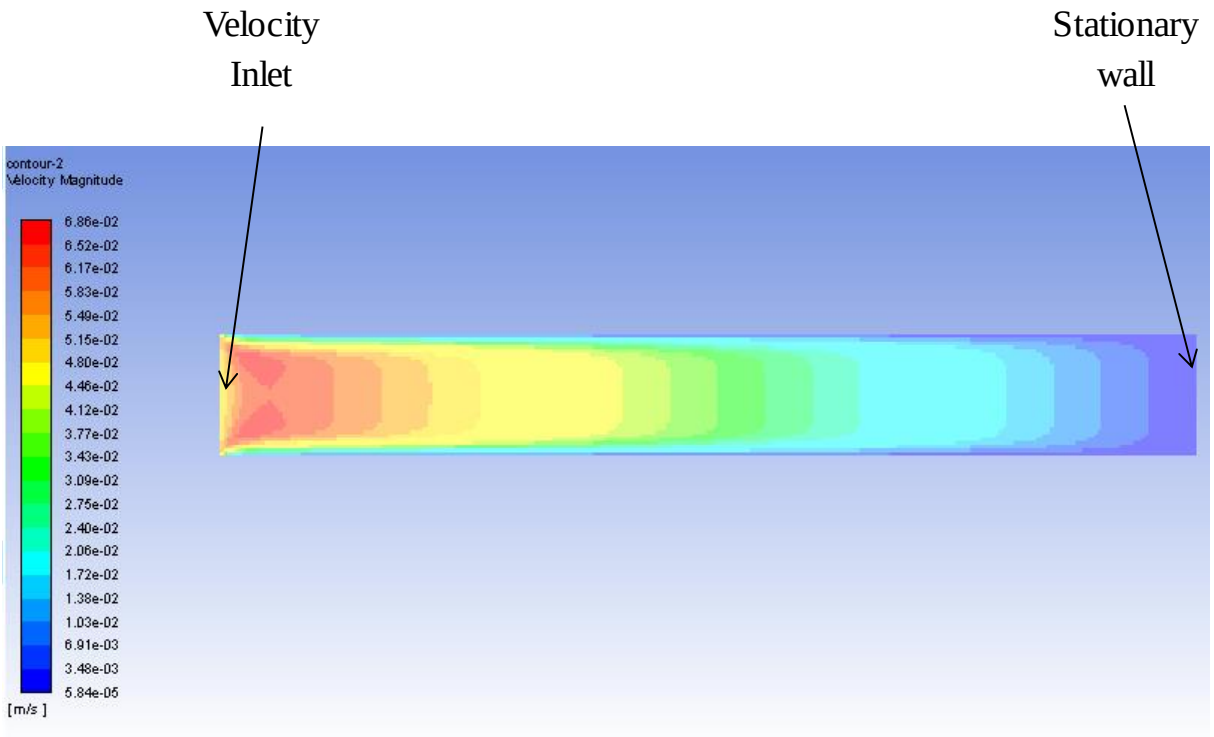

Figure S2. Velocity contour of single phase liquid in a micro-channel with velocity inlet at the left end and stationary wall at the right

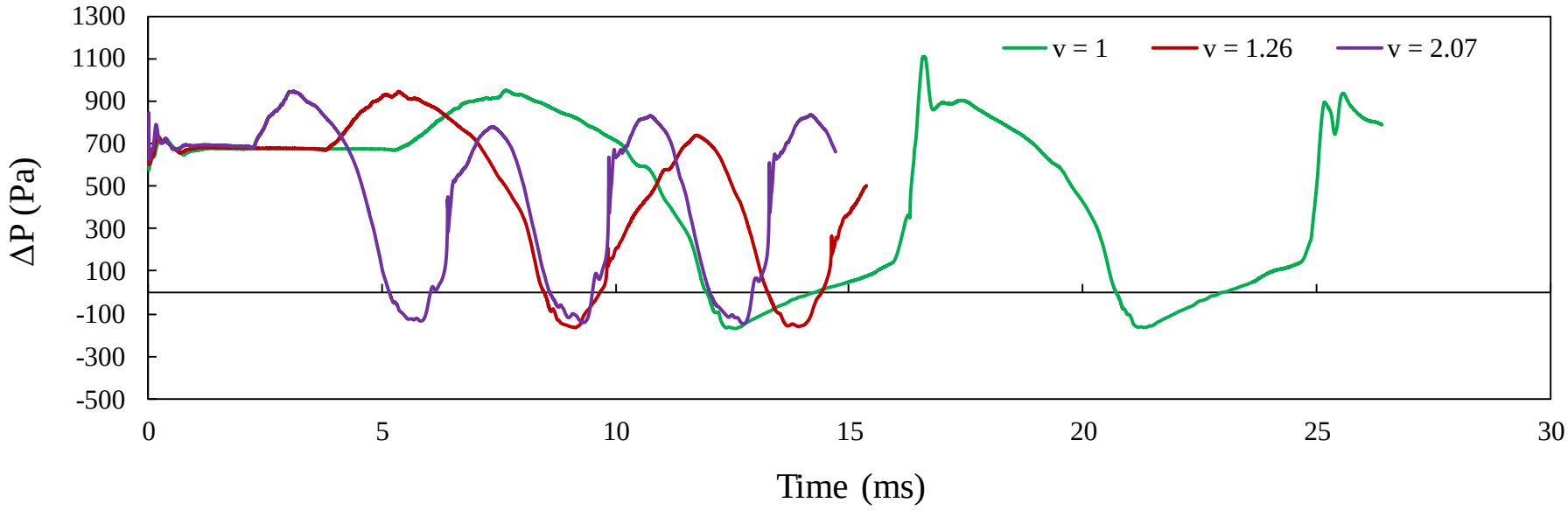

Figure S3. Pressure drop between gas and liquid inlets for different velocity ratios. Purple line: $v_g/v_l = 1$; Red line: $v_g/v_l = 1.26$; Green line: $v_g/v_l = 2.07$.

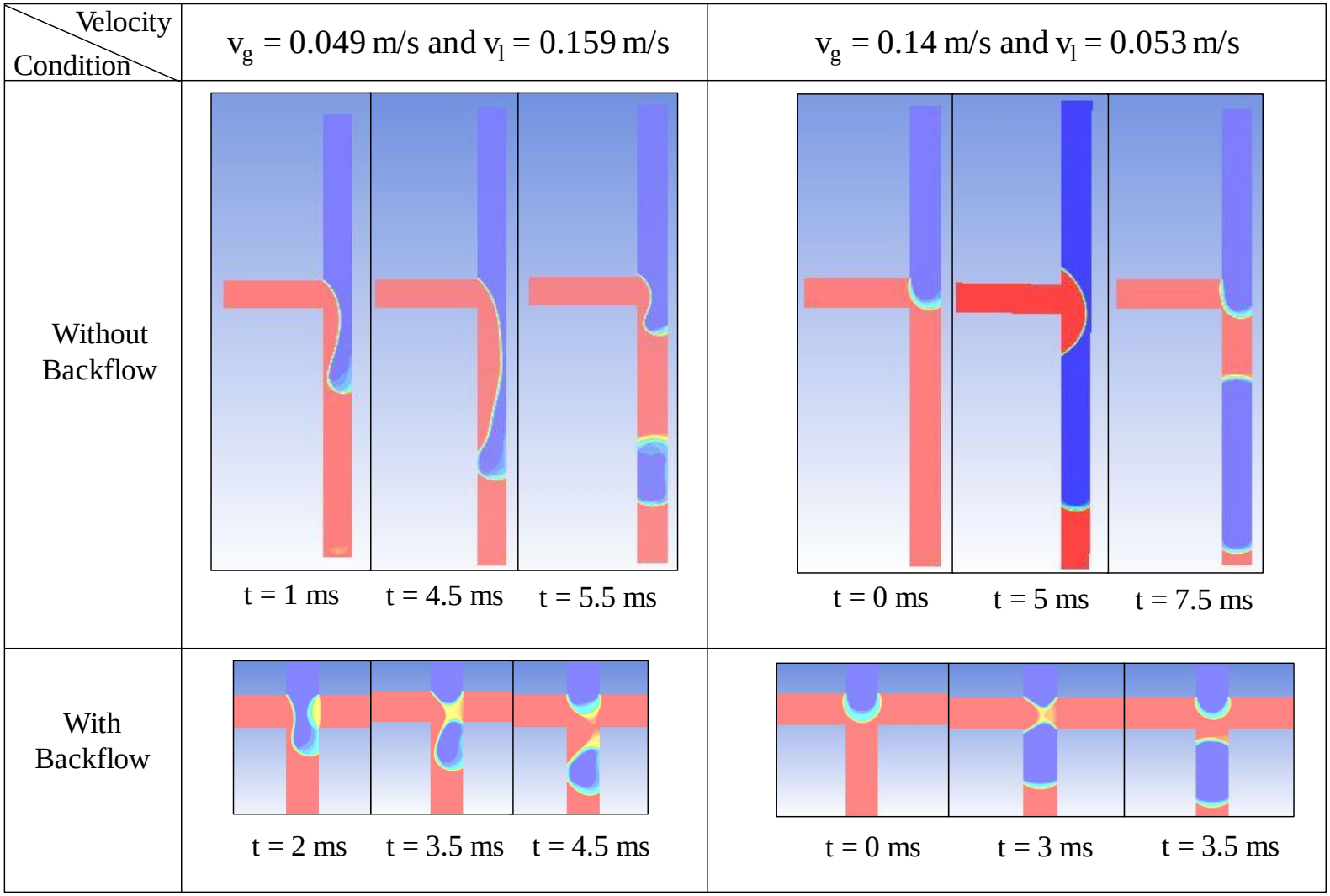

Figure S4. Comparison of microbubble formation in T-junction with and without back flow.